Journal of Applied Fluid Mechanics, Vol. 12, No. 2, pp. 361-368, 2019.
Available online at www.jafmonline.net, ISSN 1735-3572, EISSN 1735-3645.
DOI: 10.29252/jafm.12.02.28706

Aerodynamic Forces Acting on a Race Car for Various Ground Clearances and Rake Angles

I. Džijan†, A. Pašić, A. Buljac and H. Kozmar

Faculty of Mechanical Engineering and Naval Architecture, University of Zagreb, Ivana Lučića 5, 10000 Zagreb, Croatia

†*Corresponding Author Email: ivo.dzijan@fsb.hr*

(Received December 18, 2017; accepted October 15, 2018)

ABSTRACT

Computational model was developed to investigate aerodynamic forces acting on a closed-wheel race car. A particular focus was on the effects of ground clearance and rake angle on aerodynamic drag and lift forces. Computations were performed for a steady viscous fluid flow using the realizable k-ε turbulence model and non-equilibrium wall functions. The computational results indicate a strong influence of ground clearance and rake angle on aerodynamic loading of a race car. The largest drag force coefficient was obtained for the largest ground clearance. The drag force coefficient for the squatting car is larger by 5% compared to the reference case, where the both front and rear ground clearances are 100 mm. For the nose-diving car, the drag force coefficient is equal to the reference case. Increasing the ground clearance caused a negligible increase in the lift force coefficient in comparison with the reference case. A decrease in the ground clearance yielded an increase in the lift force coefficient. The largest positive lift force coefficient was obtained for a squatting car, whereas the largest negative lift force coefficient was observed for a nose-diving car. While the favorable aerodynamic downforce acting on front wheels is larger for a nose-diving car, for rear wheels it is larger for a squatting car.

Keywords: Race car; Aerodynamic drag and lift forces; Ground clearance; Rake angle; Computational simulations.

NOMENCLATURE

A	reference area
C_D	aerodynamic drag force coefficient
C_L	aerodynamic lift force coefficient
C_p	pressure coefficient
F_D	aerodynamic drag force
F_L	aerodynamic lift force
h_F	front ride height
h_R	rear ride height
p	static pressure
p_{atm}	atmospheric pressure
p_∞	freestream flow pressure
v	flow velocity
v_∞	freestream flow velocity
I	turbulence intensity
y^+	wall distance
μ_m	molecular viscosity
μ_t	turbulent viscosity
ρ	air density

1. INTRODUCTION

Traction and dynamic stability are important aspects for overall performance of race cars, e.g. Katz (1996), while increased downforce (negative lift force) enhances the car dynamic stability, McBeath (2011). These characteristics can be improved by employing various body shapes and add-on devices, e.g. Ha *et al.* (2011), Bruneau *et al.* (2012), Kang *et al.* (2012), Buljac *et al.* (2015).

The general goal is to decrease the adverse aerodynamic drag force and to increase the favorable downforce (negative aerodynamic lift force). A decrease in the aerodynamic drag force reduces the energy consumption of a car, Paterson *et al.* (2016), Wang *et al.* (2016), while the rear shape of the car is particularly important for aerodynamic drag force, Wang *et al.* (2014).

The ground clearance and flow incidence angle of the aerodynamic devices such as front wing prove to particularly affect aerodynamic forces

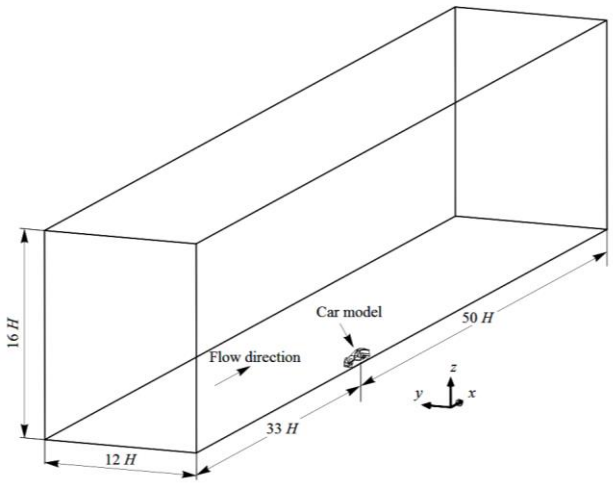

Fig. 1. Schematic view of the computational domain and the car model; dimensions are given with respect to the height of the car model.

Table 1 Boundary conditions on the surfaces of the computational domain

Inlet surface	Outlet surface	Top and lateral surfaces	Bottom surface	Car surface
Uniform profile, v_∞ = 40 m/s, I = 2 %, μ_t / μ_m = 10	$p = p_{atm}$	Symmetry walls	Moving wall with $v = v_\infty$, without a boundary layer	No-slip condition

experienced by race cars, e.g. Roberts *et al.* (2015). The front and rear parts of a car commonly have different ground clearances. This yields a certain rake angle of a car, which is important to enhance the favorable downforce of open-wheel race cars, Zhang *et al.* (2006). It is anticipated that the ground clearance and rake angle may influence aerodynamic forces for closed-wheel race cars as well, which topic is the focus of the present study.

2. Computational Setup

The studied vehicle is the XR GTR closed-wheel race car. Front and rear ground clearances of the car were determined in the center of the front and rear axles. Aerodynamic drag and lift forces were computed for ground clearance ranging from 60 mm to 140 mm with respect to the ground surface, with an increment of 20 mm. This yields 25 different test cases.

Different front and rear ground clearances yield a non-zero rake angle, which may be positive in case the rear ground clearance is larger than the front ground clearance (nose-diving), whereas it is negative for larger front ground clearance (squatting). Nose-diving car position is characteristic for heavy braking, while the squatting position is characteristic for heavy acceleration of the car.

As the computational model of the car and flow conditions were adopted to be symmetric in the lateral direction perpendicular to the main flow direction, the flow was simulated on one car side only. The obtained results were then implemented on the other car side. The dimensions of the computational domain are reported in Fig. 1 with respect to the car height H.

The dimensions of the computational domain were large enough to assure that the domain boundaries did not influence the obtained results, in agreement with Hucho (1998). The blockage corrections were not performed, as the blockage calculated as a ratio of the frontal area of the car and the frontal area of the computational domain was only 0.35 % and thus could be neglected, e.g. West and Apelt (1982). The boundary conditions applied to the surfaces of the computational domain are summarized in Table 1.

The bottom surface of the computational domain was treated as a translate-moving wall without the boundary layer development. The translational velocity of this wall was equal to the freestream flow velocity. This allowed for the development of the boundary layer on the vehicle surface, but not on the road surface, Elofsson and Bannister (2002), Huminic and Huminic (2017). As a matter of fact, a boundary layer development on the road may adversely influence the boundary layer on the vehicle body, which is particularly exhibited for vehicles with low ground clearances, Katz (1996).

Computational domain discretization was conducted using the hybrid approach, i.e. the boundary layer was discretized using five layers of

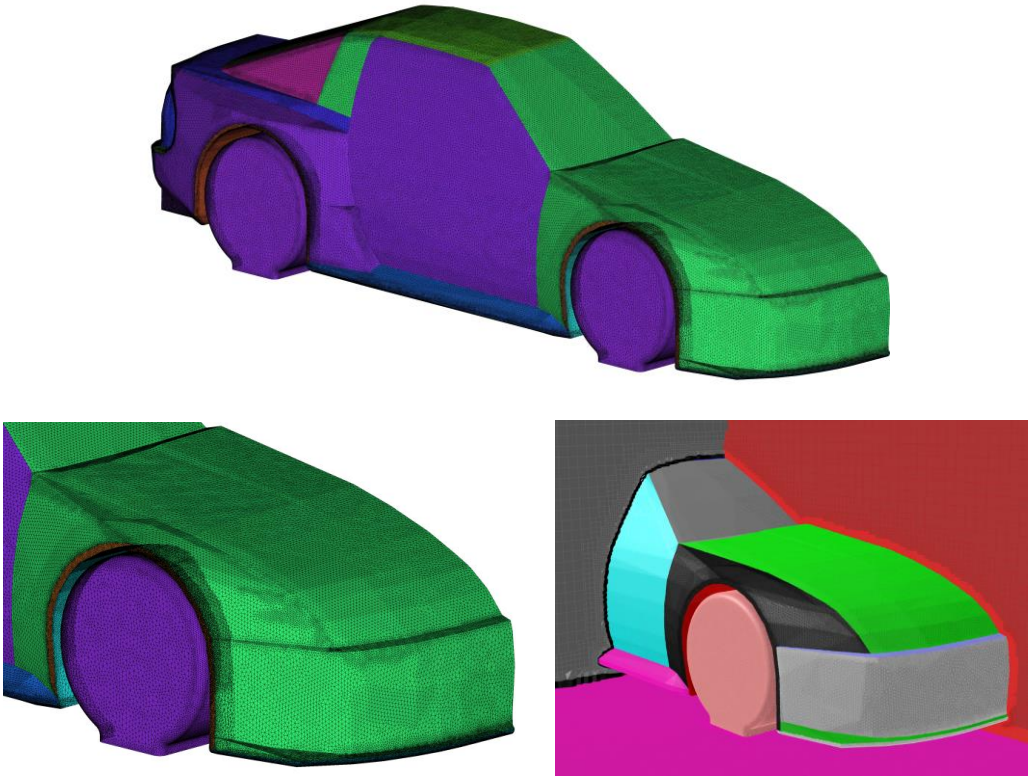

Fig. 2. Details of the geometrical discretization of the computational domain.

prismatic elements with a growth factor of 1.2, while a layer of tetrahedral elements connected the boundary layer mesh with the rest of the domain, which was discretized using hexahedral elements.

Prismatic layer elements were geometrically placed in the main flow direction, as to reduce numerical diffusion, Fig. 2. The height of the first prismatic element and the subsequent centroid distance of the cell from the wall was determined by the size of the underlying surface mesh triangular element, using a First Aspect Ratio method with a value of 5 in TGrid, thus yielding the maximal non-dimensional wall distance $y^+ \approx 150$. The total number of control volumes was 6.2 millions.

Non-equilibrium wall functions were used in the vicinity of the car surface, as to take into account local variations of the viscous layer thickness when calculating the turbulence kinetic energy. Computations were performed for steady viscous fluid flow using the Reynolds-averaged Navier Stokes (RANS) equations and the realizable k-ε turbulence model, as this model proved to be adequate for the analysis of the flow around cars, e.g. TienPhuc *et al.* (2016). The governing equations of the used RANS model are given as,

a) Continuity equation:

$$\frac{\partial \bar{v}_j}{\partial x_j} = 0, \tag{1}$$

b) Momentum equation:

$$\frac{\partial}{\partial x_j}\left(\bar{v}_j \bar{v}_i\right) = -\frac{\partial \bar{p}}{\partial x_i} + \frac{\partial}{\partial x_j}\left[\mu\left(\frac{\partial \bar{v}_i}{\partial x_j} + \frac{\partial \bar{v}_j}{\partial x_i}\right) + \right.$$
$$\left. + \mu_t\left(\frac{\partial \bar{v}_i}{\partial x_j} + \frac{\partial \bar{v}_j}{\partial x_i}\right) - \frac{2}{3}\rho \bar{k}\delta_{ij}\right]. \tag{2}$$

The mean air flow velocity is defined as $\bar{v}_i$, the coordinates are x_i, $\bar{p}$ is averaged air pressure, μ_t is turbulent viscosity, $\bar{k}$ is averaged turbulence kinetic energy defined as $\bar{k} = \frac{\overline{v_i' v_i'}}{2}$, the turbulence viscosity is defined as $\mu_t = C_\mu \rho \frac{\bar{k}^2}{\bar{\varepsilon}}$, where $\bar{\varepsilon}$ is averaged dissipation of turbulence kinetic energy, C_μ was not constant but calculated using k and ε. This numerical model was used together with two additional transport equations of the realizable k- ε turbulence model,

$$\frac{\partial}{\partial t}\left(\rho \bar{k}\right) + \frac{\partial}{\partial x_j}\left(\rho \overline{v_j}\, \bar{k}\right) = \frac{\partial}{\partial x_j}\left[\left(\mu + \frac{\mu_t}{\sigma^k}\right)\frac{\partial \bar{k}}{\partial x_j}\right] + G - \rho\bar{\varepsilon}, \tag{3}$$

$$\frac{\partial}{\partial t}\left(\rho \bar{\varepsilon}\right) + \frac{\partial}{\partial x_j}\left(\rho \overline{v_j}\, \bar{\varepsilon}\right) = \frac{\partial}{\partial x_j}\left[\left(\mu + \frac{\mu_t}{\sigma_\varepsilon}\right)\frac{\partial \bar{\varepsilon}}{\partial x_j}\right] + \tag{4}$$
$$+ \rho C_1 S \bar{\varepsilon} - C_2 \rho \frac{\bar{\varepsilon}^2}{\bar{k} + \sqrt{\nu\varepsilon}} + C_{1\varepsilon}\frac{\bar{\varepsilon}}{\bar{k}} C_{3\varepsilon}.$$

G is generation of turbulence kinetic energy, $C_{1\varepsilon}$, C_2

and $C_{3\varepsilon}$ are standard model coefficients, $S = \sqrt{2S_{ij}S_{ij}}$, $S_{ij} = \frac{1}{2}\left(\frac{\partial v_j}{\partial x_i} + \frac{\partial v_i}{\partial x_j}\right)$.

Non-segregated pressure-based coupled solver was used together with the SIMPLE algorithm to allow for faster convergence of the results. Computations were performed using the ANSYS Fluent commercial software. The undisturbed freestream air velocity in all simulations was 40 m/s. The characteristic length for calculation of the Reynolds number was the car wheelbase of 2.45 m, as recommended by the SAE (Society of Automotive Engineers) convention for cars. This yielded the Reynolds number approximately equal to $6.7*10^6$, which is larger than the critical Reynolds number for road vehicles, e.g. Hucho (1998). The aerodynamic lift F_L and drag F_D forces acting on the car are reported as dimensionless force coefficients, respectively,

$$C_D = \frac{F_D}{\frac{1}{2}\rho v_\infty^2 A}, \tag{5}$$

$$C_L = \frac{F_L}{\frac{1}{2}\rho v_\infty^2 A}. \tag{6}$$

Reference area A used to normalize aerodynamic forces was calculated as a frontal area of the vehicle perpendicular to the main (x) flow direction. The dimensionless pressure coefficient C_p was calculated as,

$$C_p = \frac{p - p_\infty}{\frac{1}{2}\rho v_\infty^2}, \tag{7}$$

As to validate the developed computational model and used geometrical discretization, the grid dependence test was conducted for the commonly used generic Ahmed body, which is similar to the race car that was the focus of the present study. The dimensions of the Ahmed body are presented in Fig. 3. The incidence angle of the rear surface was 25°, which corresponds to the shape of the studied race car. Computational domain discretization for the Ahmed body was conducted using the hybrid approach, i.e. the same approach as for the investigated race car, Figure 4. Four different meshes were created to analyze the grid independence of the obtained computational results.

The realizable k-ε turbulence model was used, as suggested in Lanfrit (2005). The aerodynamic force coefficients in Meile *et al.* (2011) are C_D = 0.299 and C_L = 0.345. In the present study they are C_D = 0.298 and C_L = 0.364 for the most coarse grid used in the validation study with 1.1 million of control volumes, thus indicating a strong similarity with Meile *et al.* (2011). Due to the adopted hybrid approach for the discretization method, the computational results correspond well to Meile *et al.* (2011) even for the most coarse grid. Furthermore, the results for the configuration with enhanced wall functions and relatively small y^+ did not yield satisfactory results, hence the non-equilibrium wall functions were used for further analysis.

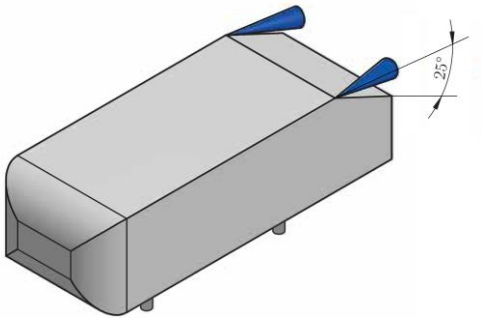

Fig. 3. Generic Ahmed reference body used to validate the computational model.

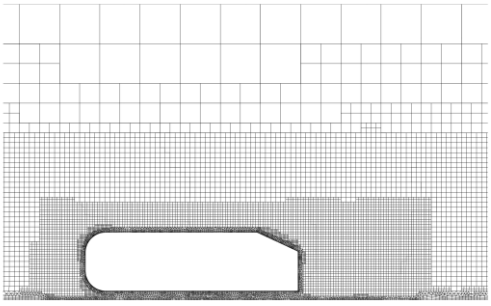

Fig. 4. Geometrical discretization of the Ahmed reference body using the hybrid approach.

The experimentally obtained flow patterns in a, b and c planes in the wake of the Ahmed body obtained by Ahmed *et al.* (1984) were qualitatively compared to the results obtained in the present validation study, Fig. 5. The experimental results by Ahmed *et al.* (1984) are reported on the left-hand side of panels a, b and c, the computational results obtained in the present study are reported on the right-hand side of those same panels.

The results show that the characteristic flow patterns reported in Ahmed *et al.* (1984) are successfully obtained in the present study as well.

3. COMPUTATIONAL RESULTS

The drag force coefficient of the studied car is reported in Fig. 6 for various front (h_F) and rear (h_R) ground clearances. The drag force coefficient for the reference case (h_F = h_R = 100 mm, zero rake angle) is 0.286. The drag force coefficient is influenced by the front and rear ground clearances of the car. The largest drag force coefficient is obtained for the largest ground clearance, while the minimal drag force coefficient is obtained for the smallest ground clearances. When compared to the reference case (h_F = h_R = 100 mm), the drag force coefficient increased by 8% for h_F = h_R = 140 mm, or decreased by 24% for h_F = h_R = 60 mm. This indicates that a simultaneous increase in h_F and h_R of similarly aerodynamically shaped closed-wheel

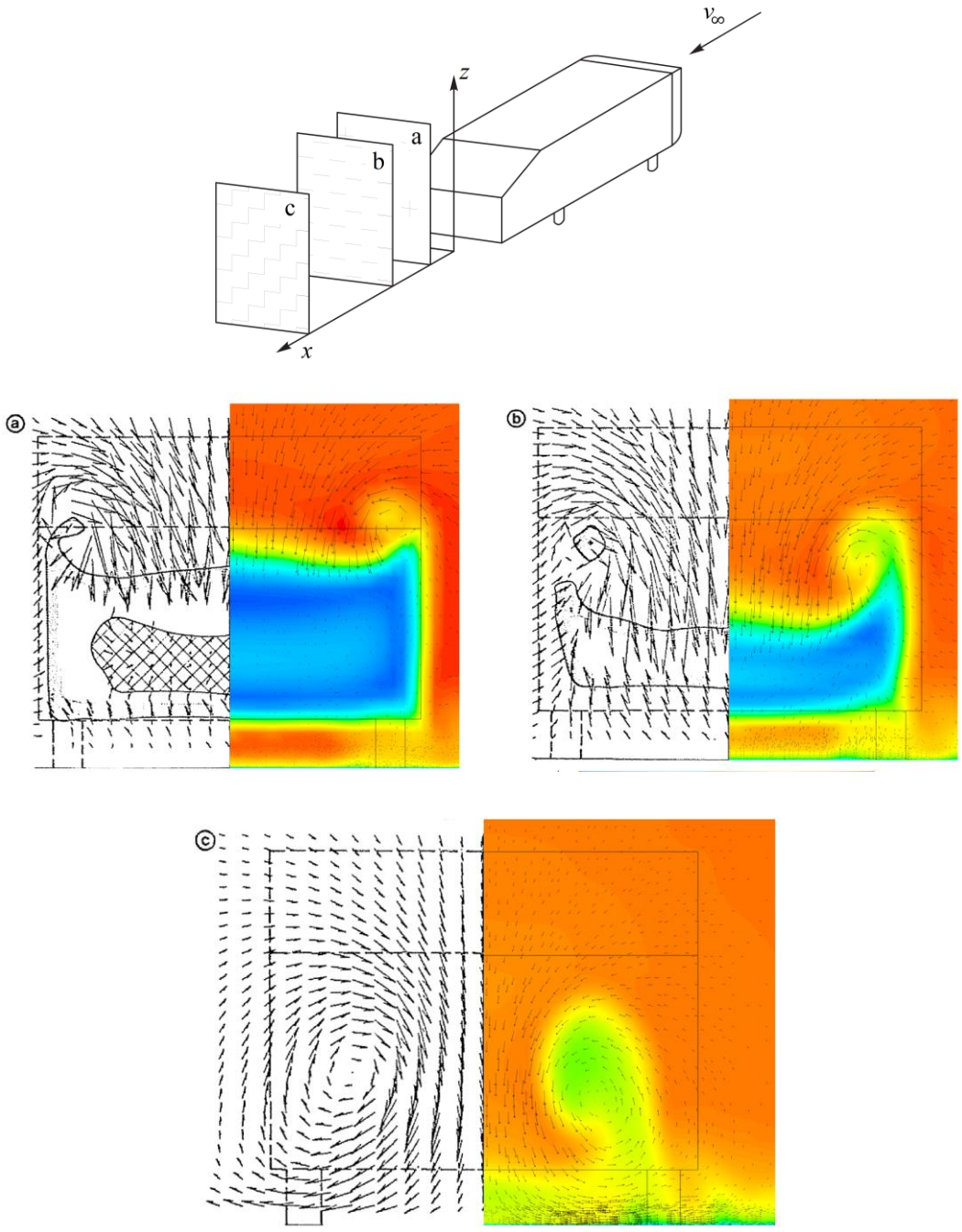

Fig. 5. Characteristic flow patterns around the Ahmed body reported for three different planes.

race cars increases the drag force coefficient. The drag force coefficient for h_F = 140 mm and h_R = 60 mm (squatting car with maximum negative rake angle) is larger by 5% when compared to the reference case. On the other hand, the drag force coefficient for h_F = 60 mm and h_R = 140 mm (nose-diving car with maximum positive rake angle) is equal to the drag force coefficient in the reference case.

The maximum studied negative rake angle (h_F = 140 mm, h_R = 60 mm) can be reduced by decreasing h_F, in which case the drag force coefficient decreases, or this can be obtained by increasing h_R, in which case the drag force coefficient increases.

The maximum studied positive rake angle (h_F = 60 mm, h_R = 140 mm) can be reduced by increasing h_F, in which case the drag force coefficient increases. The same can be achieved by decreasing h_R, in which case the drag force coefficient decreases.

The lift force coefficients of the studied car are reported in Fig. 7 for various front (h_F) and rear (h_R) ground clearances.

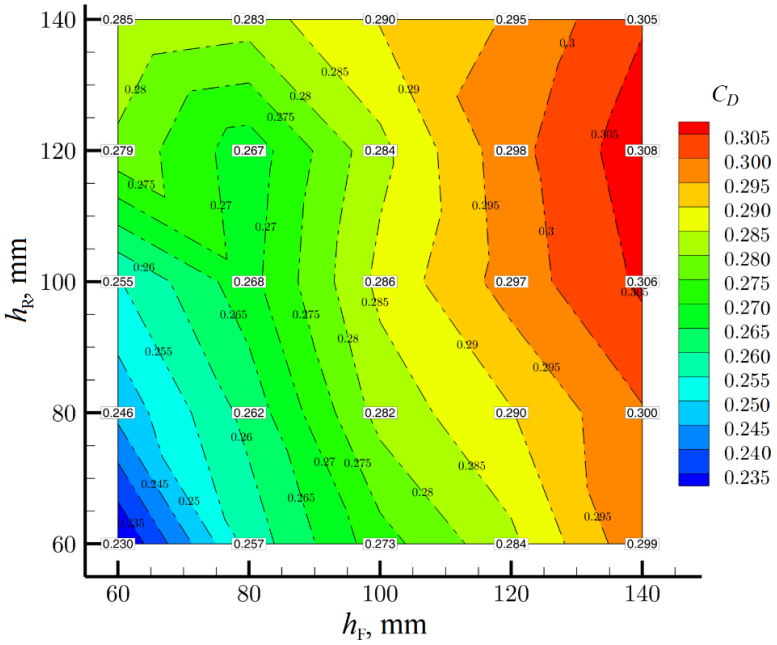

Fig. 6. Drag force coefficient for various front and rear ground clearances of the car.

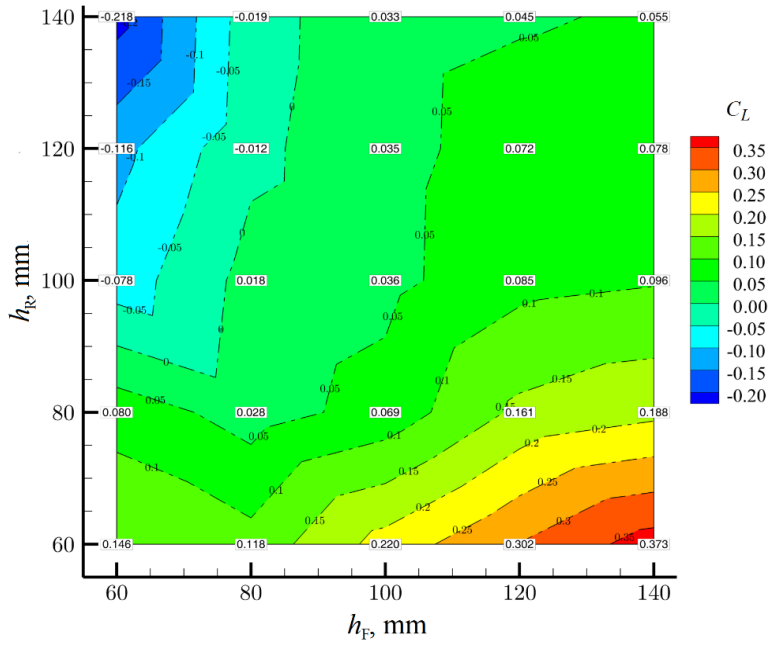

Fig. 7. Lift force coefficient for various front and rear ground clearances of the car.

The lift force coefficient of the reference case is 0.036. Increasing simultaneously h_F and h_R negligibly increases the lift force coefficient, while simultaneously decreasing h_F and h_R may significantly increase the lift force coefficient. This suggests that decreasing the ground clearance while maintaining the zero rake angle may increase the positive lift force coefficient and thus decrease the dynamic stability of the similarly aerodynamically shaped closed-wheel race cars.

The lift force coefficient is significantly altered for the car with a non-zero rake angle.

The largest positive lift force coefficient of 0.37 is obtained for the maximum negative rake angle (squatting car), while the largest negative lift force coefficient of -0.21 is obtained for the maximum positive rake angle (nose-diving car).

If the maximum studied negative rake angle (h_F = 140 mm, h_R = 60 mm) is reduced by either decreasing h_F, or by increasing h_R, the absolute value of the positive lift force coefficient decreases. In case the maximum studied positive rake angle (h_F = 60 mm, h_R = 140 mm) reduced by either decreasing h_R, or by increasing h_F, the absolute value of the negative lift force

coefficient decreases and may become positive as well.

Ground clearance and rake angle of the car thus prove to significantly influence the lift force coefficient of the studied car. This is likely due to the influence of h_F and h_R on the surface pressure distribution at the bottom surface of the car, Fig. 8. The C_p distribution at the bottom surface of the car is strongly affected by changes in h_F and h_R.

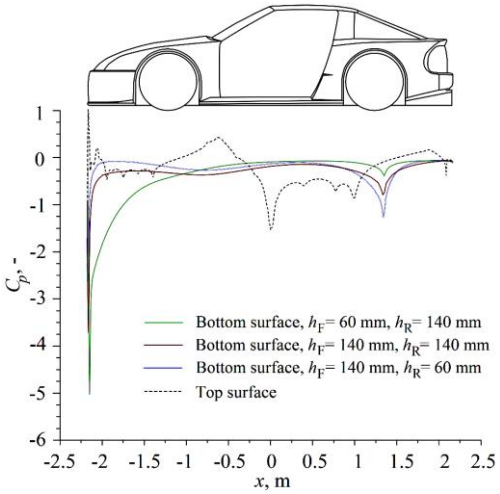

Fig. 8. C_p pressure coefficient in the car symmetry plane along the car length.

In the front part of the car ($-2.3 < x < -1$), the largest negative C_p values are obtained for a nose-diving car, while the absolute values of negative C_p results are smaller for a squatting car. This indicates that, for the similarly aerodynamically shaped race car, the aerodynamic downforce acting on front wheels is larger for a nose-diving car than for a squatting car.

In the middle part of the car ($-1 < x < 1$), the differences in C_p values are not significant for various configurations, while the absolute values are generally negative and close to zero.

In the rear part of the car ($1 < x < 2.3$), the largest negative C_p values are obtained for a squatting car, while the smallest absolute values of negative C_p results are observed for a nose-diving car. This suggests that, for a similarly aerodynamically shaped race car, the downforce acting on rear wheels is larger for a squatting car than for a nose-diving car.

The influence of the rake angle is observed on the C_p pressure coefficients at the bottom surface of the car (car undertray). On the left hand side of Fig. 9, the distribution of C_p pressure coefficients is presented for h_F = 60 mm, h_R = 140 mm, while on the right hand side C_p pressure coefficients are shown for h_F = 140 mm, h_R = 140 mm.

The C_p pressure coefficients on the bottom surface of the car are influenced by the rake angle. The lower C_p pressure coefficients are obtained for h_F = 60 mm, h_R = 140 mm (nose-diving car) than for h_F = 140 mm, h_R = 140 mm, which is particularly exhibited in the windward part of the car undertray.

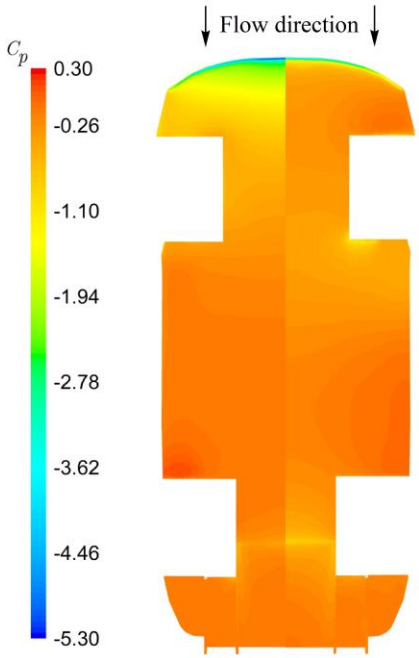

Fig. 9. C_p pressure coefficient at the bottom surface of the car for two different rake angles.

4. CONCLUSION

Aerodynamic forces acting on a closed-wheel race car were studied using Computational Fluid Dynamics with a particular focus on the ground clearance and rake angle effects. Computations were performed for a steady viscous fluid flow using the realizable k-ε turbulence model and non-equilibrium wall functions. The front and rear ground clearances proved to considerably influence aerodynamic drag and lift forces experienced by the car.

The drag force coefficient is observed to increase with increasing the ground clearance. For a squatting car (h_F = 140 mm, h_R = 60 mm, negative rake angle), the drag force coefficient is larger by 5% compared to the reference case (h_F = h_R = 100 mm, zero rake angle). On the other hand, the drag force coefficient obtained for a nose-diving car (h_F = 60 mm, h_R = 140 mm, positive rake angle) is equal to the reference case.

The lift force coefficient for the reference case is 0.036. Increasing simultaneously h_F and h_R negligibly increases the absolute value of the lift force coefficient, while simultaneously decreasing h_F and h_R may notably increase the absolute value of the lift force coefficient. The largest positive lift force coefficient of 0.37 is obtained for a squatting car, while the largest negative lift force coefficient of -0.21 is calculated for a nose-diving car.

The pressure coefficient distribution indicates that, for a similarly aerodynamically shaped race car, the aerodynamic downforce acting on front wheels is larger for a nose-diving car than for a squatting car. The downforce acting on rear wheels is larger for a squatting car than it is for a nose-diving car.

REFERENCES

Ahmed, S. R., G. Ramm and G. Faltin (1984). Some salient features of the time-averaged ground vehicle wake. *SAE Technical Paper Series* 840300, 2-31.

Bruneau, C.H., E. Creusé, D. Depeyras, P. Gilliéron and I. Mortazavi (2012). Active and passive flow control around simplified ground vehicles. *Journal of Applied Fluid Mechanics* 5(1), 89-93.

Buljac, A., I. Džijan, I. Korade, S. Krizmanić and H. Kozmar (2015). Automobile aerodynamics influenced by airfoil-shaped rear wing. *International Journal of Automotive Technology* 17(3), 377-385.

Elofsson, P. and M. Bannister (2002). Drag reduction mechanisms due to moving ground and wheel rotation in passenger cars. *SAE Paper* 2002-01-0531.

Ha, J., S. Jeong and S. Obayashi (2011). Drag reduction of a pickup truck by a rear downward flap. *International Journal of Automotive Technology* 12, 369-374.

Hucho, W. H. (1998). *Aerodynamics of road vehicles*. SAE Books International, Hamburg, Germany.

Huminic, A. and G. Huminic (2017). Aerodynamic study of a generic car model with wheels and underbody diffuser. *International Journal of Automotive Technology* 18, 397-404.

Kang, S. O., S. O. Jun, H. I. Park, K.S. Song, J. D. Kee, K.H. Kim and D.H. Lee (2012). Actively translating a rear diffuser device for the aerodynamic drag reduction of a passenger car. *International Journal of Automotive Technology* 13(4), 583-592.

Katz, J. (1996). *Race car aerodynamics*. Bentley Publishers, Cambridge, UK.

Lanfrit, M. (2005). *Best practice guidelines for handling automotive external aerodynamics with Fluent*. Fluent Deutschland GmbH White Paper.

McBeath, S. (2011). *Competition car aerodynamics*. Haynes Publishing, Bristol, UK.

Meile, W., G. Brenn, A. Reppenhagen, B. Lechner and A. Fuchs (2011). Experiments and numerical simulations on the aerodynamics of the Ahmed body. *CFD Letters* 3, 33-39.

Paterson, S., P. Vijayaratnam, C. Perera and G. Doig (2016). Design and development of the Sunswift eVe solar vehicle: a record-breaking electric car. *Proceeding of the Institution of Mechanical Engineers, Part D: Journal of Automobile Engineering* 230(14), 1972-1986.

Roberts, L.S., J. Correia, M.V. Finnis and K. Knowles (2015). Aerodynamic characteristics of a wind-and-flap configuration in ground effect and yaw. *Proceeding of the Institution of Mechanical Engineers, Part D: Journal of Automobile Engineering* 230(6), 841-854.

TienPhuc, D., G. ZhengQi and C. Zhen (2016). Numerical simulation of the flow field around generic Formula One. *Journal of Applied Fluid Mechanics* 9(1), 443-450.

Wang, Y., W. Cheng, T. Gangfeng and Y. Deng (2016). Reduction in the aerodynamic drag around a generic vehicle by using a non-smooth surface. *Proceeding of the Institution of Mechanical Engineers, Part D: Journal of Automobile Engineering* 231(1), 130-144.

Wang, Y., Y. Xin, Zh. Gu, Sh. Wang, Y. Deng and X. Yang (2014). Numerical and experimental investigations on the aerodynamic characteristics of three typical passenger vehicles. *Journal of Applied Fluid Mechanics* 7 (4), 659-671.

West, G. S. and C. J. Apelt (1982). The effects of tunnel blockage and aspect ratio on the mean flow past a circular cylinder with Reynolds numbers between 10^4 and 10^5. *Journal of Fluid Mechanics* 114, 361-377.

Zhang, X., W. Toet and J. Zerihan (2006). Ground effect aerodynamics of race cars. *Applied Mechanics Reviews* 59(1), 33-49.